Flow Around Ships Sailing in Shallow Water
- Experimental and Numerical Results

X.-N. Chen, A. Gronarz, S. List
(Versuchsanstalt für Binnenschiffbau e.V. Duisburg)
N. Stuntz
(Gerhard-Mercator-Universität Duisburg)

ABSTRACT

In this paper the results of the investigation of the flow around the models of two ships in shallow water without propeller, rudder and appendices are presented. The intention is - based on reliable experimental data - to compare computational results from different methods, obtained on different grids, and see how these methods perform. The experimental measurements comprise the velocity field at several stations, the free surface deformation, the hull pressure distribution and (not presented in this contribution) the bottom pressure. Three different computational methods were applied: A standard RANSE-solver on two different grids (one block-structured hexaedral, one unstructured tetraedral), a RANSE-solver using a fictitious compressibility and thus a flux-difference-splitting technique and a potential theoretic method devised for the transcritical regime (solitons!), where the hull is described merely by its cross-sectional area.

INTRODUCTION

In this paper the special characteristics of the flow around ships sailing in shallow water are demonstrated for two hull forms.

Though there is no well defined limit for the water depth h dividing shallow from deep water, the behaviour of waves is well known to depend on the depth h. The behaviour of vessels sailing in shallow water may be characterized by the dimensionless number F_{nh}, the depth Froude number, defined as:

$$F_{nh} = \frac{V}{\sqrt{g \times h}}$$

with V the speed of the ship and g the gravitational acceleration. F_{nh} clearly rules the wave resistance of the ship, by representing the ratio of V to the so called critical velocity $\sqrt{g \times h}$ leading thus to a division of the whole velocity range into a subcritical and a supercritical region depending on F_{nh} being smaller or larger than 1, in similarity with what happens at high velocities in air, where the velocity of sound is the critical velocity, separating the subsonic from the supersonic range. The velocity range of V with values of $0.9 < F_{nh} < 1.1$ is termed the transcritical range. So the rather pronounced change in the magnitude of the wave resistance is characterized by a single number, while the situation for the viscous resistance is different, as there is no critical velocity and therefore no number similar to F_{nh}.

From values of $F_{nh} \sim 0.65$ the wave resistance increases steeply for increasing velocity V becoming higher than the wave resistance on deep water at the same velocity. The wave resistance has a local maximum in the transcritical region where although the speed of the ship being kept constant, no steady flow regime may be attained, while so called solitons detach from the hull running ahead of the ship. If the vessel is forced into the supercritical range, the wave resistance becomes lower than the one which would be obtained at the same speed in deep water.

A key parameter for the influence of the water depth on the resistance is the depth to draft ratio h/d. For $h/d < 4$ there appear first changes even in the viscous resistance for velocities corresponding to values of $F_{nh} < 0.5$ due to a different distribution of the flow around the hull.

The VBD, Versuchsanstalt für Binnenschiffbau Duisburg, European Development Centre for Inland and Coastal Navigation, has since its foundation in 1953 been dedicated to the investigation of the shallow water effects on the behaviour of ships. This implies also the interaction of the ship with bottom and banks of the waterways, canals as well as rivers. Besides these activities on ship hydrodynamics, the ship as part of transport chains in integrated logistics solutions is investigated in the departments of Transport Economics and Transport Engineering of the VBD. For the hydrodynamic investigation, be it for the industry or in the frame of projects for research funding institutions, the VBD is equipped with excellent facilities, a shallow water towing tank (where water depth may easily be varied, current may be simulated and waves may be generated) being the central system. The department of computational fluid dynamics (CFD) backs the department of experimental fluid dynamics (EFD).
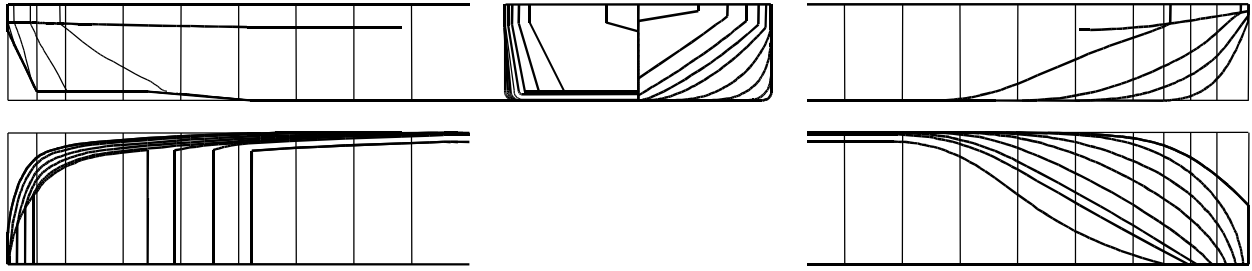
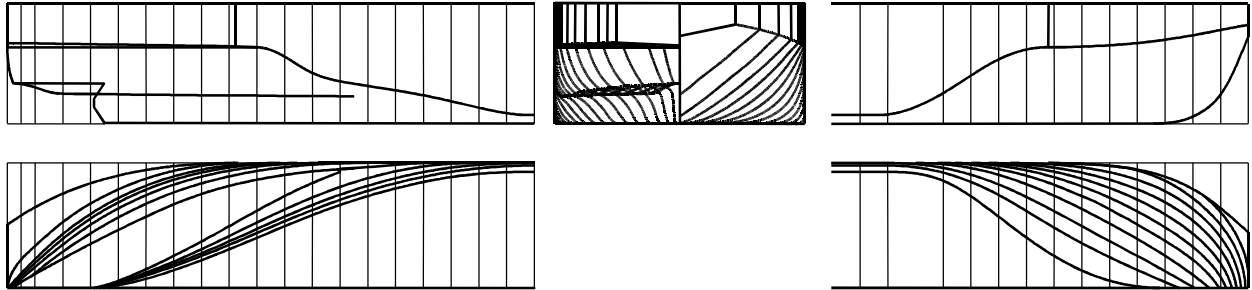Fig. 1: Lines Plan - Shallow river vessel (Ship A)

Fig. 2: Lines Plan - Inland waterway ship (Ship B)

The two selected examples of ship types are typical for the investigative performance of the VBD in both fields EFD and CFD. In both cases the emphasis is on the sailing on shallow water, and as the topic here is flow around the ship, but no allusion will be made to trim, sinkage or resistance values obtained.

MODELS INVESTIGATED

Shallow river vessel

The model investigated (Fig. 1) is a typical inland waterway ship for extreme shallow water. The stern is, as can be seen from the lines plan, designed to allow the installation of a special flat thruster system (Schottel Pump Jet), flush with the base line. Its scale was 1:12. The model was fitted with 120 pressure taps at 12 different stations. In this paper we will refer to it as Ship A. The main particulars are:

Length betw. perp.	L_{pp}	[m]	82.0
Beam	B	[m]	9.5
Draft	d	[m]	1.5
Displacement	V	[m³]	1054

Inland waterway ship

This is a single screw ship with the typical form of inland water vessels. As can be seen from Fig. 2 it has a characteristic tunneled stern, designed to ensure good water supply to the propeller. In these ships the propellers have rather small diameters and are highly loaded. Though only results for the scale 1:12.08 are presented, a series of geosim models was investigated with the scales 1 : 12.08, 1 : 14, 1 : 17.28 and 1 : 21.54. In this paper we will refer to it as Ship B. The main particulars are:

Length betw. perp.	L_{pp}	[m]	110.00
Beam	B	[m]	11.45
Draft	d	[m]	3.00
Displacement	V	[m³]	3312

EXPERIMENTS

The coordinate system used is righthanded: x-axis oriented in direction of ship motion, y-axis at right angles pointing to starboard, z-axis orthogonally upward, the origin is at the intersection of aft perpendicular with base-line.

Ship A

The wave pattern on the water surface was recorded by a series of wave probes located at appropriate y-positions and standard pressure probes were used to obtain the hull-pressure distribution for the cases

h/d	F_n	F_{nh}	R_n
1.2	0.078	0.529	$3.95*10^6$
2.0	0.098	0.512	$4.94*10^6$

The velocity field was only measured at $h/d = 2.0$ with a 3-component Laser-Doppler-Velocimetry (LDV) system, specifically designed to be used in shallow water tests.

Ship B

Here we will deal only with the model at the scale 1 : 12.08, comparing some results obtained in the shallow-water towing-tank with computational results. Results are presented for the h/d values

h/d	F_n	F_{nh}	R_n
1.5	0.1376	0.6302	$1.097*10^7$
3.0	0.1803	0.6805	$1.437*10^7$

Deformation of the free surface and hull pressure were determined as in Ship A, while for the survey of the velocity field (5 sections in the stern region) a spherical 5-hole pressure probe was used.

CFD-METHODS APPLIED

RANSE-Solver CFX-5 from AEA Technology (Methods 1 & 2)

This solver applies the finite volume-element method. Several turbulence models of the scalar eddy-viscosity type or a Reynolds-stress model may be chosen. Here the choice between block- structured hexaedral (Method 1) as well as completely unstructured grids with tetraedral meshes (Method 2) is an appealing feature. A mesh refinement in (eventually nested) regions is easily performed for the unstructured grid. For the detailed characteristics and features available consult the specification sheet provided by AEA Technology (N.N., 1999).

The volume meshes for calculations carried out with both methods had the expansions

Method	Ship	h/d	Vertices	Elements
1 (Hex)	A	1.2	244.462	222.010
1 (Hex)	A	2.0	283.269	263.452
2 (Tet)	A	2.0	261.625	1.342.842
2 (Tet)	B	1.5	156.498	747.313

RANSE-Solver based on the principle of artificial compressibility (Method 3)

This is a finite volume method using a structured grid. Introducing an artificial compressibility a coupling of the so obtained continuity equation to the momentum equations is achieved, allowing an efficient Roe flux-difference-splitting technique. The method includes the computation of the free water surface considered as the boundary between water and air and described by a so called level set function satisfying an additional equation (derived from the boundary condition) solved together with the above mentioned equations. The turbulence model is the standard k - e model (Stuntz, 1999).

With this method numerical calculations have been carried out, using a volume mesh comprising of 264.000 Elements (160 in longitudinal, 50 in transverse and 33 in vertical direction).

Shallow water potential-theoretic transcritical treatment (Method 4)

Applying shallow-water-wave theory and a far-field/near-field treatment with appropriate matching, an ingenious potential theoretic method was developed by Chen and Sharma (1994) and reimproved by Chen (1999) yielding a detailed description of the deformation of the free surface. An equation of a Kadomtsev-Petviashvili type for a depth averaged potential is derived for the far field and an improved slender body theory for the near field. Though the method was developed originally to cope with the instationary case of the transcritical regime (including the solitons), it is applicable over a wide range of F_{nh} numbers. The numerical solution is obtained by applying a finite difference method. The topography of the waterway bottom may vary in direction perpendicular to the direction of ship motion and the hull is represented merely by its cross-sectional area distribution and the local beam of the water line.

EFD RESULTS

Ship A

The pressure distribution on the hull is shown in dimensional form by colours and isolines on the hull surface. The location of the pressure taps is shown (red dots), Figs. 6 and 9. The results (Gronarz et al, 1994) of the three component LDV measurements are shown as arrows, Figs. 11, 14, 17 and 20. The free surface deformation is shown as colour and isoline-pattern, Fig. 21.

Ship B

The pressure distribution on the hull is shown in dimensional form by colours and isolines on the hull surface. The location of the pressure taps is shown in Fig. 23 (crosses). The velocity vector-field surveyed at five stations in the stern region is displayed for three typical sections, showing the lengthwise component as colour- and isoline-patterns and the transverse components as arrows, Figs. 31, 32 and 33. Although the positive x-coordinate is in direction of the ship motion, the x-component of the velocity has been taken as positive. The free surface deformation is shown as colour and isoline-pattern, Fig. 28 (VBD-report in preparation).

CFD RESULTS

In all the computational results the presentation of the magnitudes is chosen so as to match that of the corresponding experiment.

The area covered by the computational grids has in y-direction a much larger extension than in the figures of the velocity distribution in the transverse sectional planes (Figs. 12, 13, 14, 15, 16, 18, 19, 34, 35 and 36).

Ship A

Overview of figures showing results

	h/d	x/L_{pp}	EFD Exp.	CFD-Method 1	CFD-Method 2	CFD-Method 4
hull presssure	2		6	7	8	
hull presssure	1.2		9	10		
velocity distribution	2		20			
velocity distribution	2	0.1	11	12	13	
velocity distribution	2	0	14	15	16	
velocity distribution	2	- 0.1	17	18	19	
surface deformation	2		21			22

The computational grids for the Methods 1 and 2 (Fig. 3, 4 and 5) extends in x-direction from 1.83 L_{pp} in front to 0.45 L_{pp} behind the ship, from the water plane to the bottom and from the center plane to a channel width of 4.9 m (half breadth of VBD-tank).

The resolution used for the calculations with Method 4 (results in Fig. 22) was 60 sections for the

model, 420 cuts in front and 840 behind the ship. The tank width (9.81 m) was divided into 81 intervals.
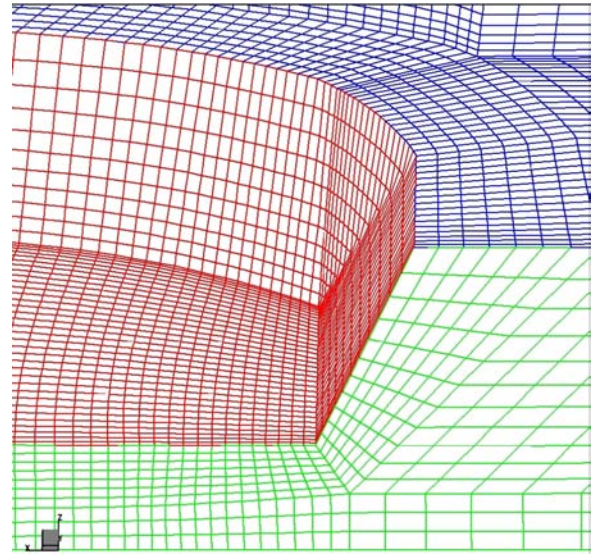
Fig. 3: Computational grid (Method 1), $h/d = 1.2$
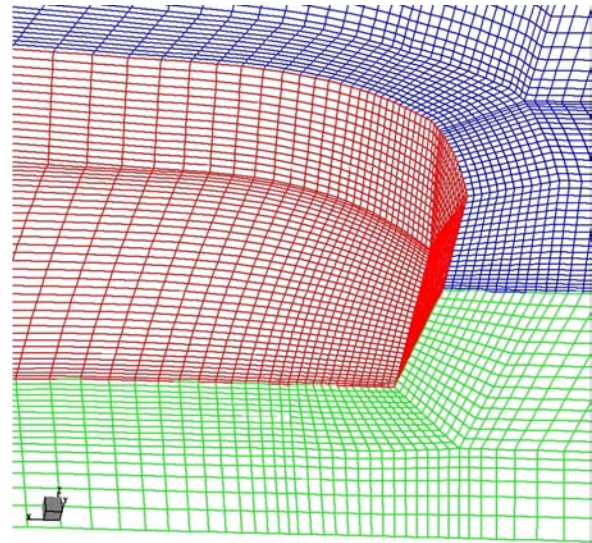
Fig. 4: Computational grid (Method 1), $h/d = 2.0$
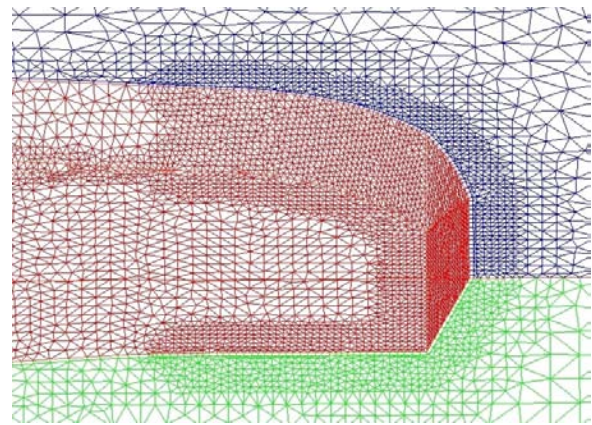
Fig. 5: Computational grid (Method 2), $h/d = 2.0$
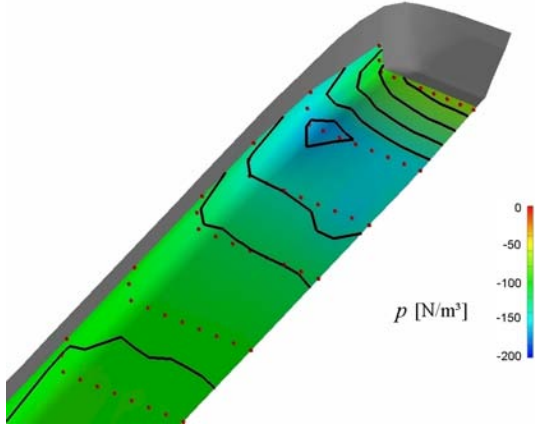
Fig. 6: Hull pressure distribution. Experimental results h/d = 2.0, F_n = 0.098, F_{nh} = 0.512, R_n = 4.94∗10⁶
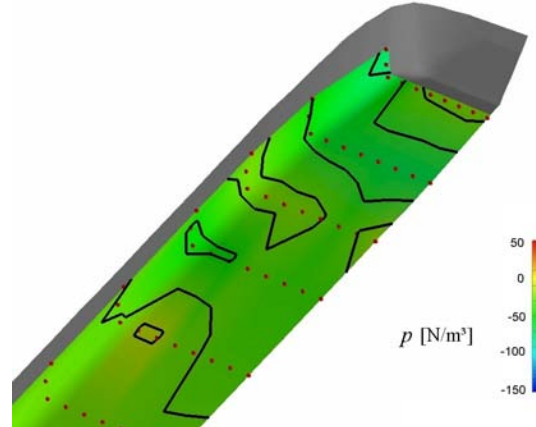
Fig. 9: Hull pressure distribution. Experimental results at h/d = 1.2, F_n = 0.078, F_{nh} = 0.529, R_n = 3.95∗10⁶
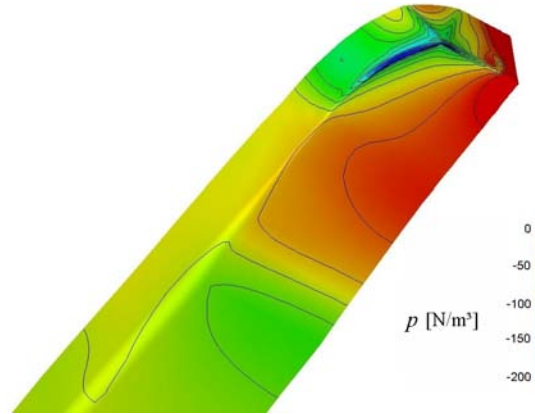
Fig. 7: Hull pressure distribution. Computational results (Method 1) h/d = 2.0, F_n = 0.098, F_{nh} = 0.512, R_n = 4.94∗10⁶
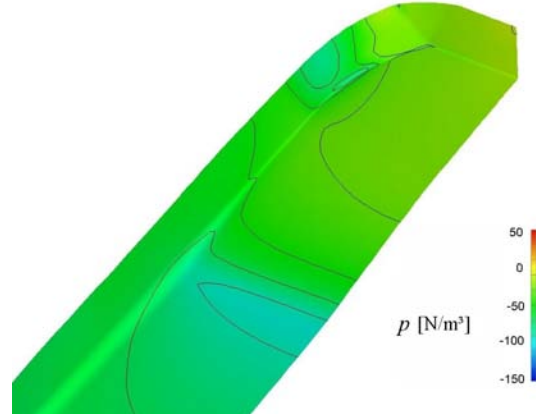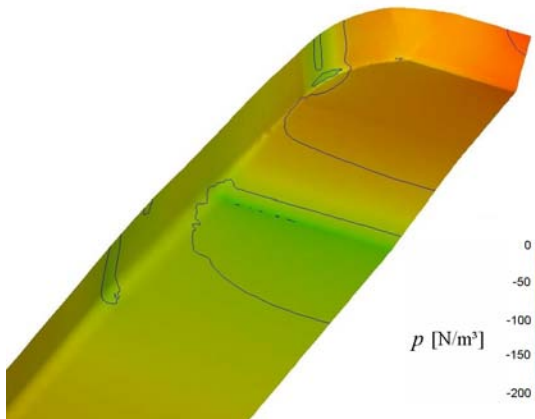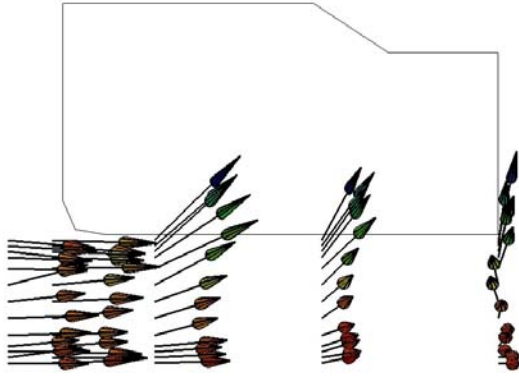

Fig. 10: Hull pressure distribution. Computational results (Method 1) h/d = 1.2, F_n = 0.078, F_{nh} = 0.529, R_n = 3.95∗10⁶

Fig. 8: Hull pressure distribution. Computational results (Method 2) at h/d = 2.0, F_n = 0.098, F_{nh} = 0.512, R_n = 4.94∗10⁶
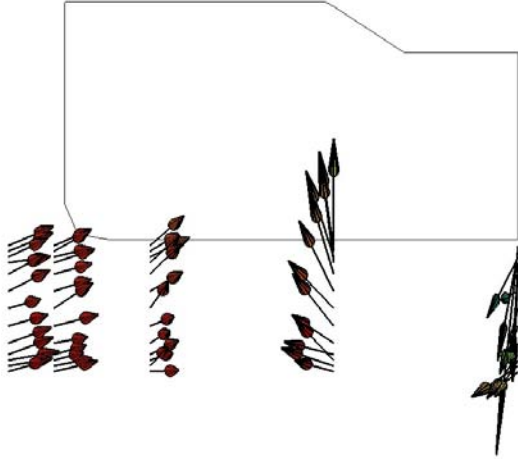
Fig. 11: Velocity distribution (stern section $x/L_{pp} = 0.1$). LDV-measurements at $h/d = 2.0$, $F_n = 0.098$, $F_{nh} = 0.512$, $R_n = 4.94*10^6$
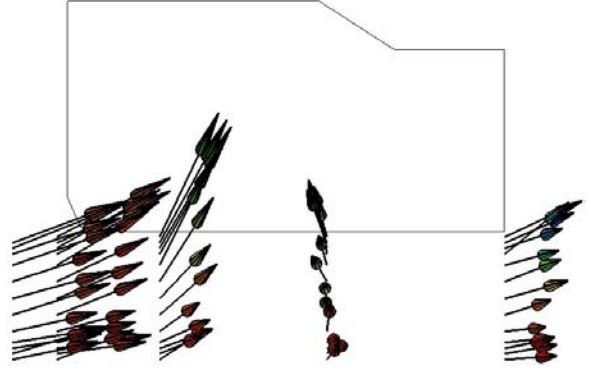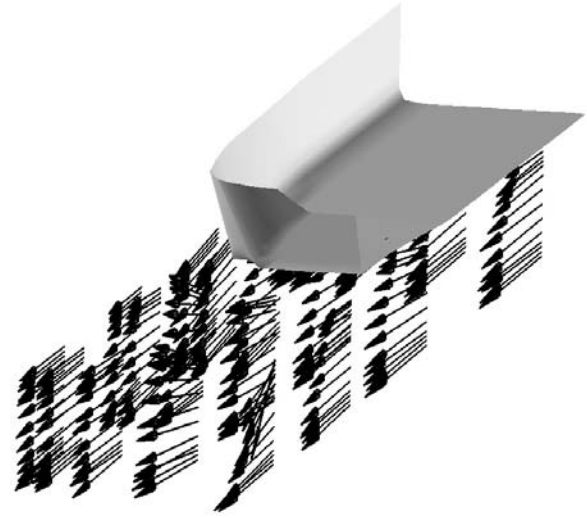

Fig. 14: Velocity distribution (stern section $x/L_{pp} = 0.0$). LDV-measurements at at $h/d = 2.0$, $F_n = 0.098$, $F_{nh} = 0.512$, $R_n = 4.94*10^6$
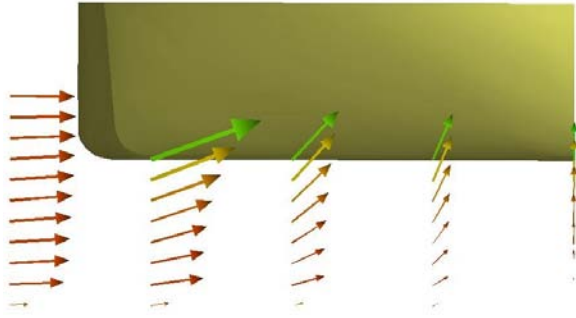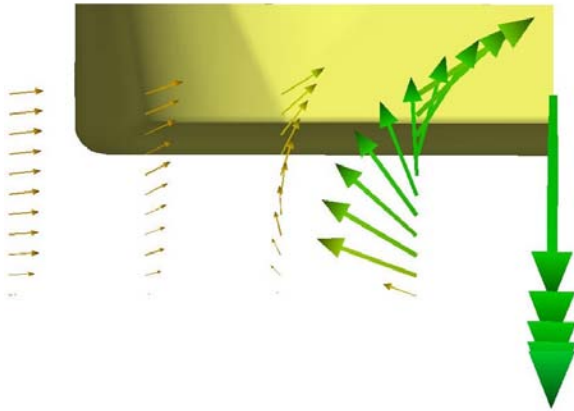

Fig. 12: Velocity distribution (stern section $x/L_{pp} = 0.1$). Computational results (Method 1) at at $h/d = 2.0$, $F_n = 0.098$, $F_{nh} = 0.512$, $R_n = 4.94*10^6$
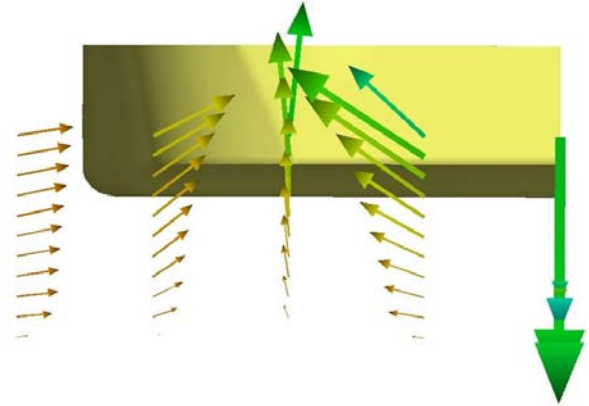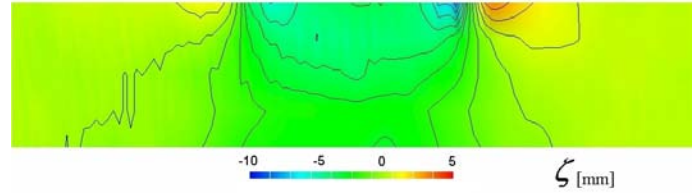

Fig. 15: Velocity distribution (stern section $x/L_{pp} = 0.0$). Computational results (Method 1) at at $h/d = 2.0$, $F_n = 0.098$, $F_{nh} = 0.512$, $R_n = 4.94*10^6$
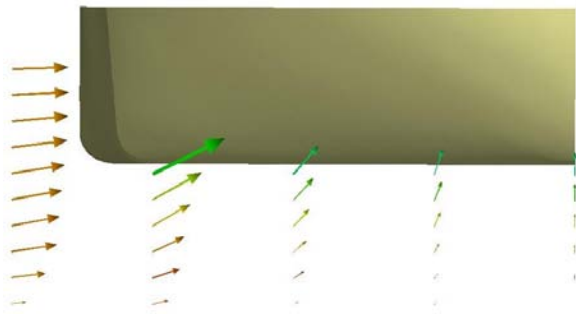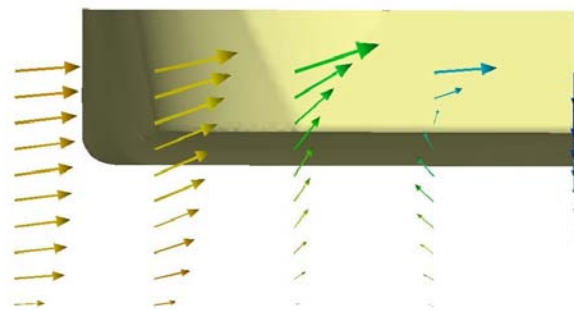

Fig. 13: Velocity distribution (stern section $x/L_{pp} = 0.1$). Computational results (Method 2) at at $h/d = 2.0$, $F_n = 0.098$, $F_{nh} = 0.512$, $R_n = 4.94*10^6$

Fig. 16: Velocity distribution (stern section $x/L_{pp} = 0.0$). Computational results (Method 2) at at $h/d = 2.0$, $F_n = 0.098$, $F_{nh} = 0.512$, $R_n = 4.94*10^6$

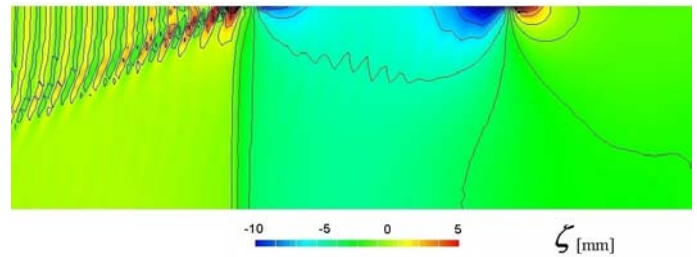The colour of the velocity vectors of the computational results for Ship B indicates the absolute value of the velocities, with warm for high and cold for low speed.

Fig. 17: Velocity distribution (stern section x/L_{pp} = -0.1). LDV-measurements at h/d = 2.0, F_n = 0.098, F_{nh} = 0.512, R_n = 4.94∗10⁶

Fig. 20: Velocity distribution (stern region). LDV-measurements at at h/d = 2.0, F_n = 0.098, F_{nh} = 0.512, R_n = 4.94∗10⁶

Fig. 18: Velocity distribution (stern section x/L_{pp} = -0.1). Computational results (Method 1) at at h/d = 2.0, F_n = 0.098, F_{nh} = 0.512, R_n = 4.94∗10⁶

Fig. 21: Water surface deformation. Experimental results at at h/d = 2.0, F_n = 0.098, F_{nh} = 0.512, R_n = 4.94∗10⁶

Fig. 19: Velocity distribution (stern section x/L_{pp} = -0.1). Computational results (Method 2) at at h/d = 2.0, F_n = 0.098, F_{nh} = 0.512, R_n = 4.94∗10⁶

Fig. 22: Water surface deformation. Computational results (Method 4) at h/d = 2.0, F_n = 0.098, F_{nh} = 0.512

Ship B

Overview of figures showing results

	h/d	x/L_pp	EFD Exp.	CFD-Method 2	CFD-Method 3	CFD-Method 4
hull presssure	1.5		23	24	25	
surface deformation	1.5		28 42		30	29 43 44
velocity distribution	1.5	.0274	31	34	37	
velocity distribution	1.5	.0640	32	35	38	
velocity distribution	1.5	.1006	33	36	39	
surface deformation	3		44			44

(Remark: The calculations with Method 3 have been carried out at $h/d = 2.0$ instead of 1.5)

The computational grid for the Method 2 (Fig. 26 on the next page) extends in x-direction from 1.5 L_{pp} in front to 0.5 L_{pp} behind the ship, from the water plane to the bottom and from the center plane to a channel width of 4.9 m (half breadth of the VBD towing tank).

The calculations with Method 3 used a structured grid (Fig. 27 on the next page) which extends in x-direction from 0.82 L_{pp} in front to 1.82 L_{pp} behind the ship, from the water plane to the bottom and from the center plane to the channel width.

The resolution used for the calculations with Method 4 (Fig. 22) was 60 sections for the model, 420 cuts in front and 840 behind the ship. The tank width (9.81 m) was divided into 61 intervals.
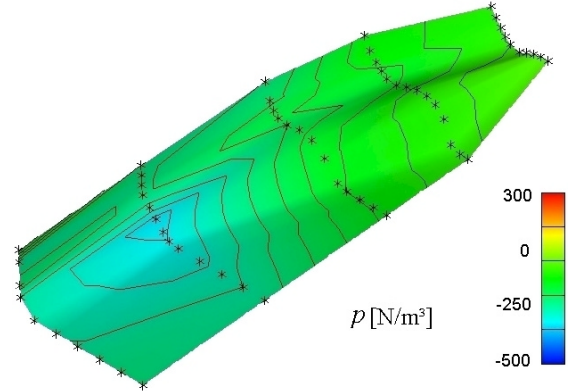
Fig. 23: Hull pressure distribution. Experimental results at $h/d = 1.5$, $F_n = 0.1376$, $F_{nh} = 0.6302$, $R_n = 1.097*10^7$
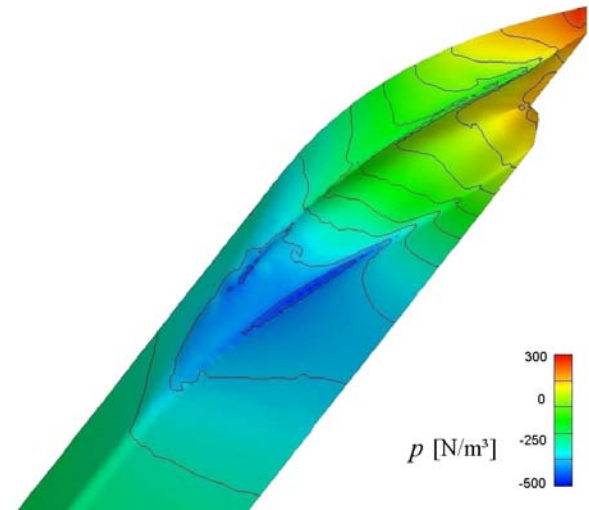

Fig. 24: Hull pressure distribution. Computational results (Method 2) at $h/d = 1.5$, $F_n = 0.1376$, $F_{nh} = 0.6302$, $R_n = 1.097*10^7$
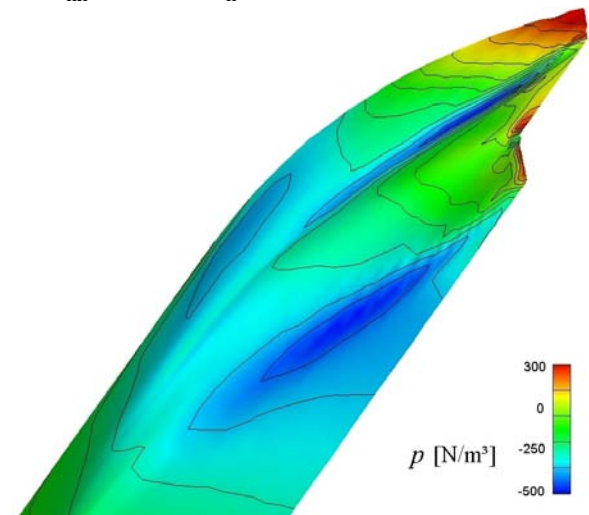

Fig. 25: Hull pressure distribution. Computational results (Method 3) at $h/d = 2.0$, $F_n = 0.1376$, $F_{nh} = 0.5458$, $R_n = 1.097*10^7$
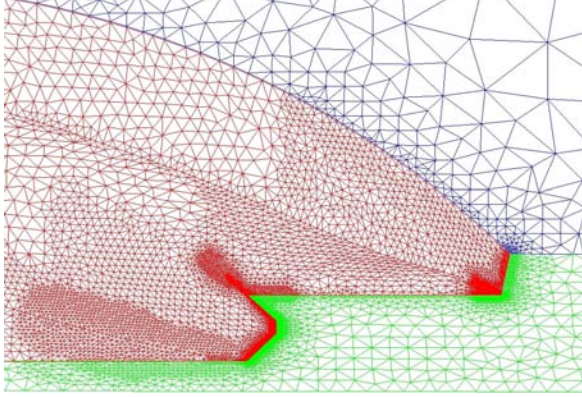
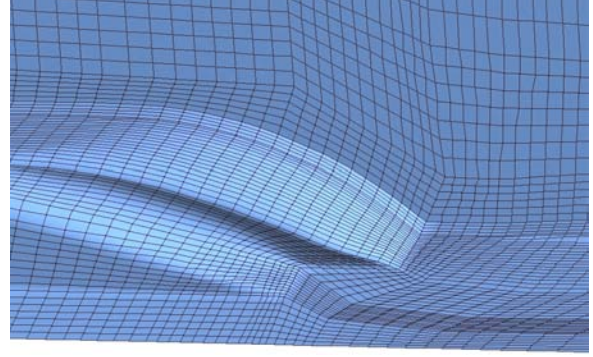Fig. 26: Computational grid (Method 2), $h/d = 1.5$
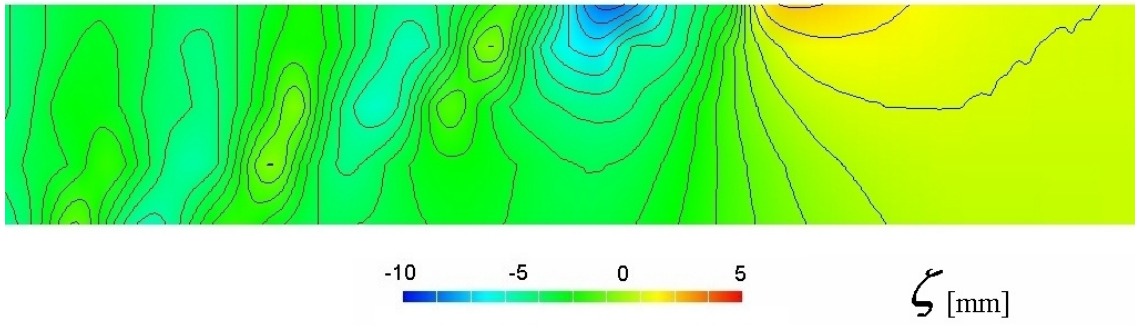

Fig. 27: Computational grid (Method 3), $h/d = 2.0$

Fig. 28: Water surface deformation z . Experimental results at $h/d = 1.5$,
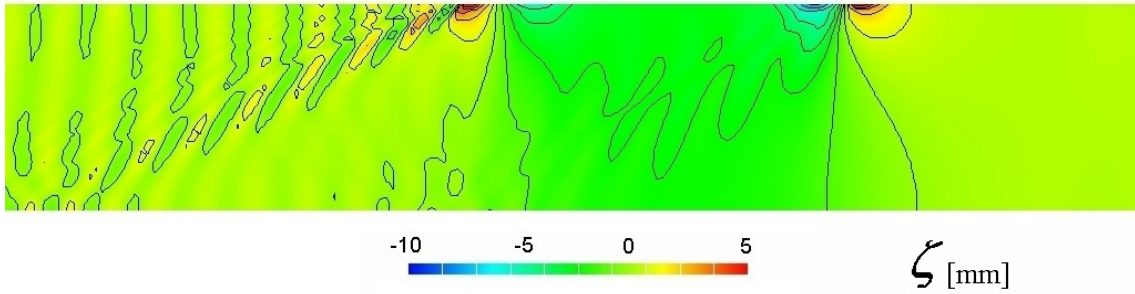$F_n = 0.1376$, $F_{nh} = 0.6302$, $R_n = 1.097*10^7$

Fig. 29: Water surface deformation z . Computational results (Method 4) at $h/d = 1.5$,
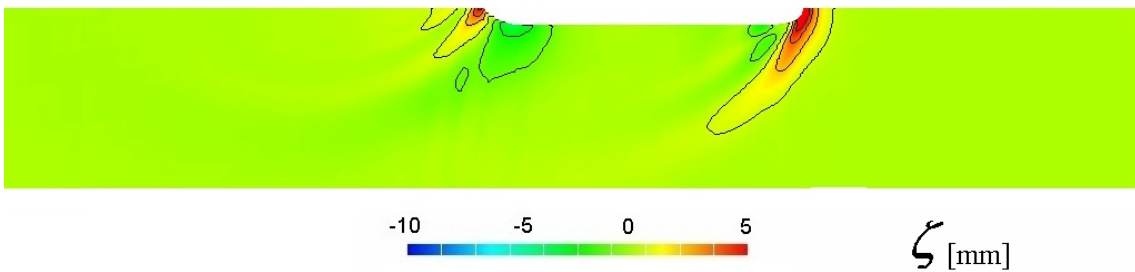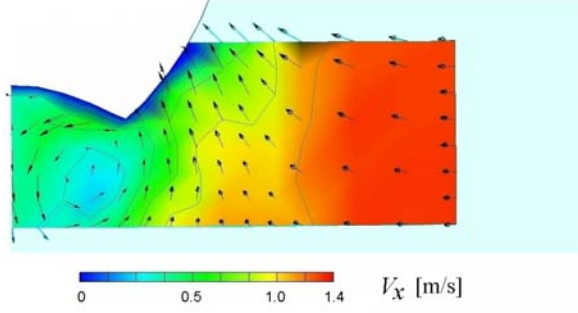$F_n = 0.1376$, $F_{nh} = 0.6302$

Fig. 30: Water surface deformation z . Computational results (Method 3) at $h/d = 2.0$,
$F_n = 0.1376$, $F_{nh} = 0.5458$, $R_n = 1.097*10^7$

Fig. 31: Velocity distribution (stern section $x/L_{pp} = 0.0274$). Experimental results (5-hole-pressure probe) at $h/d = 1.5$, $F_n = 0.1376$, $F_{nh} = 0.6302$, $R_n = 1.097*10^7$
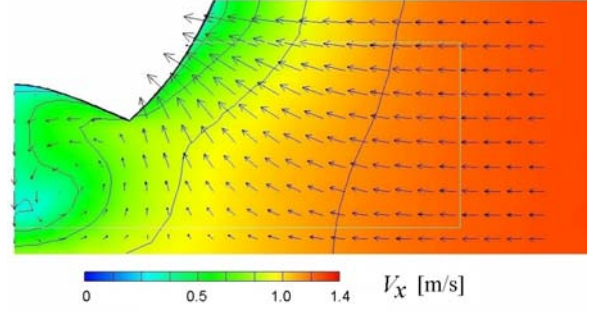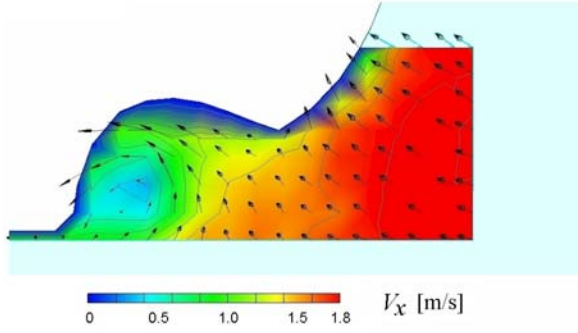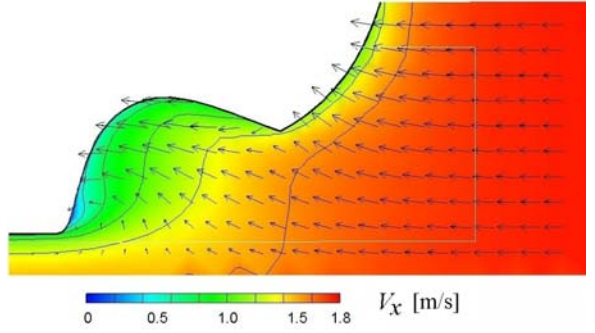

Fig. 34: Velocity distribution (stern section $x/L_{pp} = 0.0274$). Computational results (Method 2) at $h/d = 1.5$, $F_n = 0.1376$, $F_{nh} = 0.6302$, $R_n = 1.097*10^7$

Fig. 32: Velocity distribution (stern section $x/L_{pp} = 0.064$). Experimental results (5-hole-pressure probe) at $h/d = 1.5$, $F_n = 0.1376$, $F_{nh} = 0.6302$, $R_n = 1.097*10^7$

Fig. 35: Velocity distribution (stern section $x/L_{pp} = 0.064$). Computational results (Method 2) at $h/d = 1.5$, $F_n = 0.1376$, $F_{nh} = 0.6302$, $R_n = 1.097*10^7$
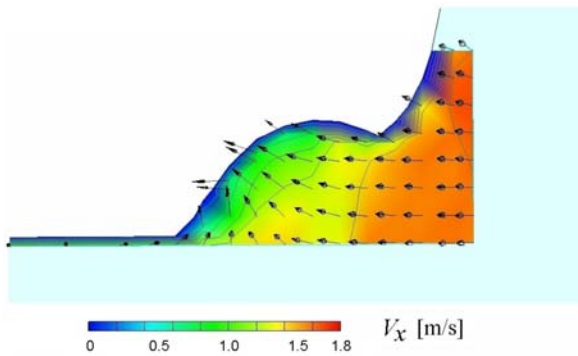

Fig. 33: Velocity distribution (stern section $x/L_{pp} = 0.1006$). Experimental results (5-hole-pressure probe) at $h/d = 1.5$, $F_n = 0.1376$, $F_{nh} = 0.6302$, $R_n = 1.097*10^7$
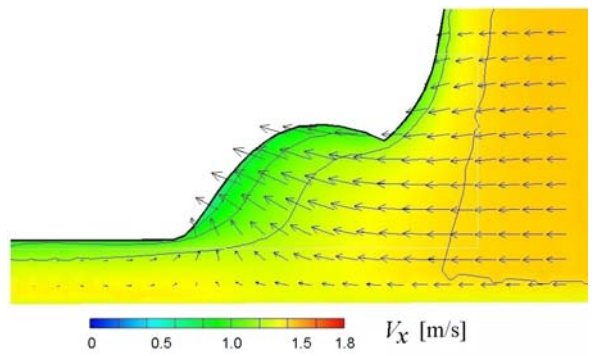

Fig. 36: Velocity distribution (stern section $x/L_{pp} = 0.1006$). Computational results (Method 2) at $h/d = 1.5$, $F_n = 0.1376$, $F_{nh} = 0.6302$, $R_n = 1.097*10^7$
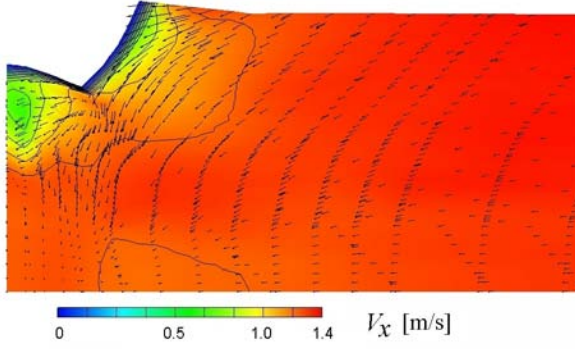
Fig. 37: Velocity distribution (stern section x/L_{pp} = 0.0274). Computational results (Method 3) at h/d = 2.0, F_n = 0.1376, F_{nh} = 0.5458, R_n = 1.097*10^7
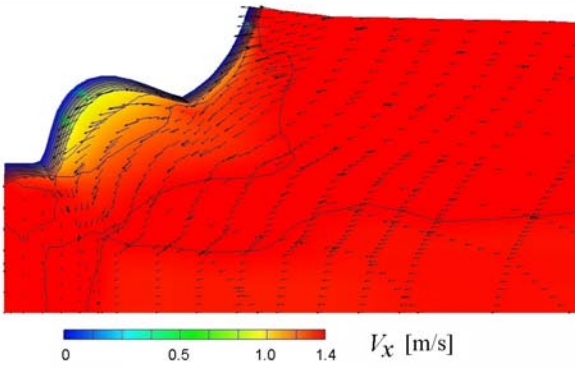

Fig. 38: Velocity distribution (stern section x/L_{pp} = 0.064). Computational results (Method 3) at h/d = 2.0, F_n = 0.1376, F_{nh} = 0.5458, R_n = 1.097*10^7
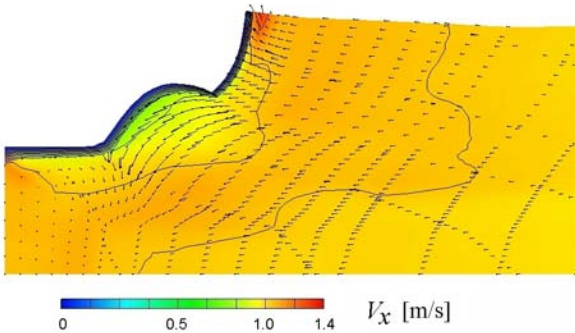

Fig. 39: Velocity distribution (stern section x/L_{pp} = 0.0274). Computational results (Method 3) at h/d = 2.0, F_n = 0.1406, F_{nh} = 0.5458 , R_n = 1.097*10^7
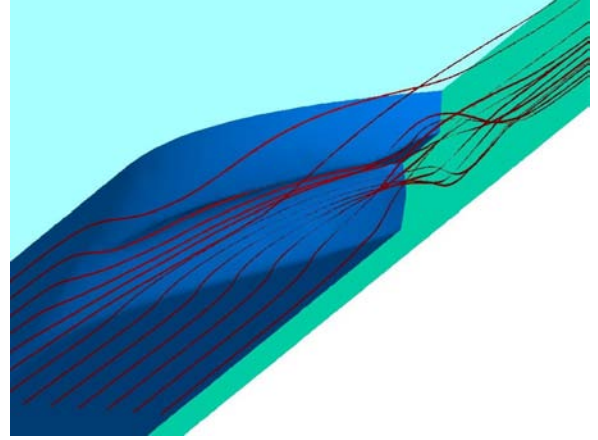

Fig. 40: Streamline visualisation by ribbons. Computational results (Method 2) at h/d = 1.5, F_n = 0.1406, F_{nh} = 0.6302, R_n = 1.097*10^7
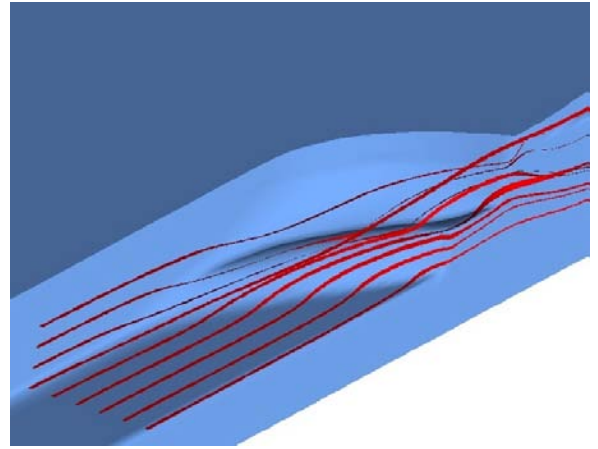

Fig. 41: Streamline visualisation by ribbons. Computational results (Method 3) at h/d = 2.0, F_n = 0.1406, F_{nh} = 0.5458, R_n = 1.097*10^7
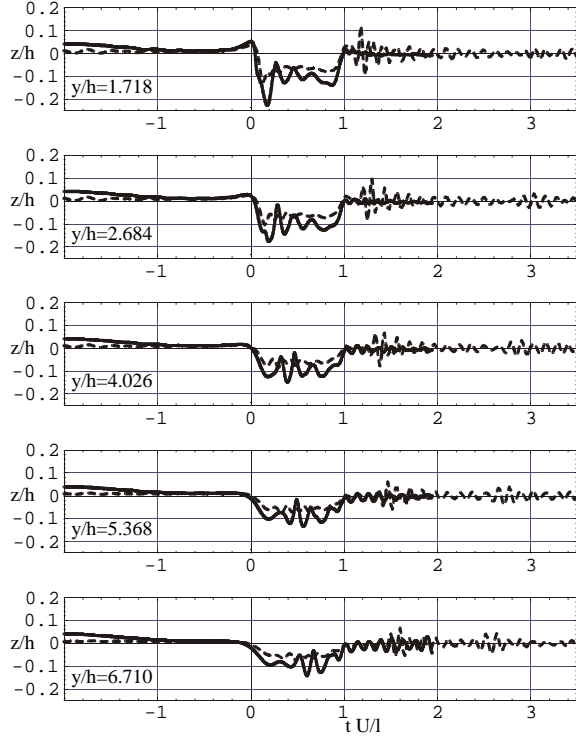
Fig. 42: Comparison of measured (solid line) and computed (dashed line, Method 4) wave cuts at $h/d = 1.5$, $F_n = 0.1406$, $F_{nh} = 0.6302$, $R_n = 1.097*10^7$

Fig. 43: Computed 3-D-wave pattern showing reflection on tank walls (Method 4) at $h/d = 1.5$, $F_n = 0.1406$, $F_{nh} = 0.6302$, [Domain comprising the full tank width, vertical scale exaggerated 8 times]
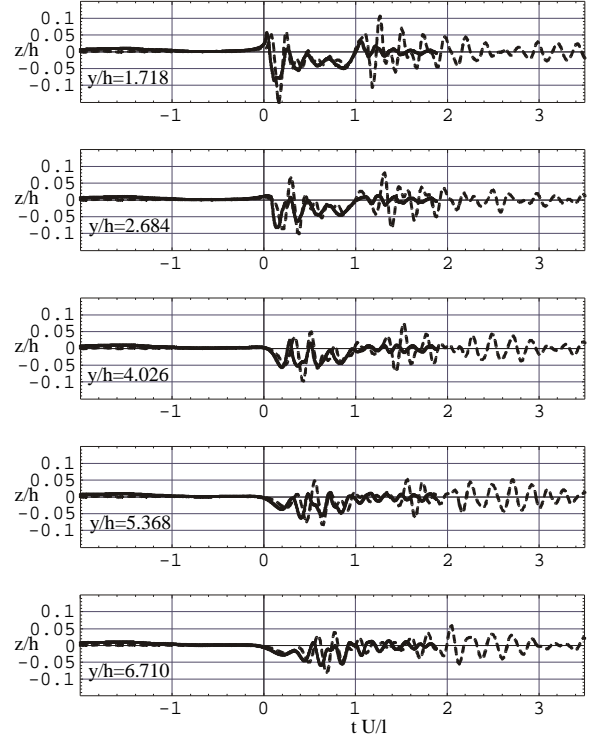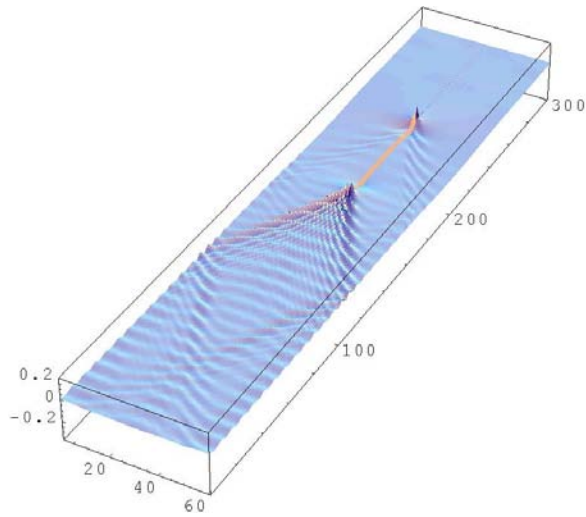

Fig. 44: Comparison of measured (solid line) and computed (dashed line, Method 4) wave cuts at $h/d = 3.0$, $F_n = 0.1803$, $F_{nh} = 0.6805$, $R_n = 1.440*10^7$

COMPARISON OF RESULTS

The correspondence between hull pressure distributions obtained by the different computational methods and between computation and experiment is dissapointing (Figs. 6, 7, 8 and 9, 10 and 23, 24, 25). This applies to both hull forms and to any of the h/d ratios presented. The computed distributions show a broader range of variability than the experimental distributions suggesting that the (three-dimensional and probably rather thick) boundary layer in the stern region has a certain equalizing effect and is probably not well reproduced in the computation. A pressure variation across the layer (contrary to the assumption for thin boundary layers) strongly dependent on the location on the hull is possibly present too but not reproduced in the computation. For Ship B in addition the experimental values as shown by the color distribution are misleading, as pressure taps were not located precisely on the sharp edges bordering the tunnels but on the sides of these edges avoiding thus likely cusps in the real pressure distribution, the interpolating postprocessing routine producing rather a smoothed distribution.

Advancing to the distribution of the velocity as a vector field we are nevertheless faced with a better correspondence. For Ship A (velocity measured by LDV at the h/d ratio 2) this is fair at the section $x/L_{pp} = 0.1$ while at the section $x/L_{pp} = 0.0$ there seems to be a suspicious deviation from symmetry in the experimental values as displayed by the arrows representing the velocity vectors in the plane $y = 0$. For Ship B (velocity measured by five-hole pressure probe at $h/d = 1.5$) the computed distributions of the velocity obtained by Method 2 in the three selected transverse planes show the characteristic vortex well known from the experiment, though its location appears slightly altered, the correspondence being somewhat better for small x/L_{pp} (Figs. 31, 34, Figs. 32, 35 and Figs. 33, 36). Due to difficulties in the generation of the structured grid for the Method 3 here an h/d ratio of 2 and not of 1.5 was chosen. The results are displayed in the Figs. 37, 38 and 39.

The deformation of the free surface is not well reproduced by the computational methods, neither for Ship A, where only results from the potential theoretic Method 4 (Fig. 22) may be compared with the experimental results (Fig. 21), nor for Ship B, where results from Method 3 (Fig. 30) and from Method 4 (Fig. 29) should match the experimental pattern (Fig. 28). The comparison of wave cuts for Ship B shown in Fig. 42 ($h/d = 1.5$) and Fig. 44 ($h/d = 3$) gives an impression of the quality attained by Method 4. The 3-D wave pattern shown in Fig. 43 demonstrates the ability to reproduce wave reflections from the side walls.

CONCLUSION

As a towing tank institution the VBD has a paramount interest in deliver reliable data to its customers. This applies nowadays as well to CFD results as it has been always expected for the EFD results. Independence of the computational grid used is one of the first achievements to be reached. We see, that for us, there remains some work to be done. In addition to model scales full scale cases should be computed too. In the future the influence of the turbulence model applied has to be clarified. So far the numerical treatment corresponds to the situation in the standard resistance test. The influence of the canal width on the flow around the ship will have to be one of the next steps. In the future the appropriately simplified simulation of the propulsor will be integrated into the computational treatment as well as rudder and appendages thus corresponding to the situation in the self-propelled-test. This will lead us to more thorough investigations of the instationary flow and the manouevring of ships in restricted water.

REFERENCES
Chen, X.-N. (1999) : *Hydrodynamics of Wave-Making in Shallow Water*, Dissertation, Faculty of Mathematics, University of Stuttgart

Chen, X.-N. and Sharma, S. D. (1994) : *Nonlinear theory of asymmetric motion of a slender ship in a shallow channel*. 20th Symp. on Naval Hydrodynamics (ONR), Santa Barbara, California, National Academy Press, Washington, D.C.

Gronarz, A., Grollius, W., Rieck, K. and Pagel, W. (1995) : *Experimentelle und theoretisch-numerische Strömungsuntersuchungen an Binnenschiffen*. VBD-report no. 1366

Bet, F., Stuntz, N., Hänel, D. and Sharma, S.D. (1999) : *Numerical Simulation of Ship Flow in Restricted Water*. 7th International Conference on Numerical Ship Hydrodynamics, Nantes

Grotjans and Menter (1998) : *Wall Functions for General Application CFD Codes*, ECCOMAS 98, Fourth European Computational Fluid Dynamics Conference, Athen

N.N. (1999) : *Using CFX-5 for Unix & Windows NT*, User manual from AEA Technologies, Harwell, UK